Supplementary Information

Facet-Dependent Metal-Support Interactions in Cobalt-Ceria Binary Oxides: Linking Ceria Morphology (rods vs. cubes) to Redox Behaviour and CO Oxidation

Agapi Orfanoudaki, [a] *Maria Lykaki,* [a] *Angelos K. Bonis,* [b] *Shailza Saini,* [b] *George Dury,* [c] *Greg A. Mutch,* [c] *Evangelos I. Papaioannou,* [c] *Kalliopi Kousi* [b] *and Michalis Konsolakis ** [a]

[a.] *School of Production Engineering and Management, Technical University of Crete, Chania, Greece.*

[b.] *School of Chemistry and Chemical Engineering, University of Surrey, Guildford, United Kingdom.*

[c.] *Materials, Concepts & Reaction Engineering (MatCoRE) Group, School of Engineering, Newcastle University, Newcastle upon Tyne, UK.*

*Corresponding author: Prof. Dr Michalis Konsolakis (mkonsolakis@tuc.gr).

Materials characterization

N_2 adsorption-desorption experiments were performed at –196 °C using a Physisorption Analyzer (NOVA 800, Anton Paar QuantaTec, Inc., Boynton Beach, Florida 33426, USA). Prior to the measurements, the samples were degassed at 150 °C for 1 h and 250 °C for 5 h under vacuum. Total surface area was determined via multipoint BET method and the total pore volume was determined at p/po ≈ 0.99. The mesopores size distribution was determined via the Barrett-Joyner-Halenda (BJH), using the desorption branch data.

XRD measurements were conducted at room temperature using a PANalytical X'Pert Pro diffractometer equipped with Cu Kα radiation (operated at 30 mA and 40 kV). Diffraction patterns were obtained over a 2θ range of 10° to 90°, with a scan rate of 0.011° s^{-1} and a step size of 0.013°. XRD patterns were obtained for freshly prepared catalysts. The average crystallite size (D_{XRD}) was calculated using the Scherrer equation (Eq. S1):[1]

$$D_{XRD} = \frac{K * \lambda}{\beta * \cos\theta} \qquad (S1)$$

where D presents the average crystallite size in nm, K is the shape factor (taken as 0.9 in this study), λ denotes the X-ray wavelength, β is the full width at half maximum (FWHM) of the diffraction peak measured in radians, and θ is the Bragg angle in degrees.

SEM images were captured using a Thermo Fisher Apreo2 SEM operated at 2 kV and 0.1 nA. TEM was conducted using a Thermo Fisher Talos F200i, equipped with a 200 kV electron source. Elemental analysis was carried out using an energy-dispersive X-ray spectroscopy (EDS) system (Bruker X-Flash Dual 100 mm^2 detector). For TEM sample preparation, the powder was ultrasonically dispersed in ethanol and drop-cast onto copper grids with a lacey carbon film, followed by drying.

Raman measurements were conducted using a Horiba LabRAM HR Evolution Raman spectrometer (exciting line wavelength, λ = 532 nm, source power 455 mW). A non-dispersive filter was used to reduce the power at the sample to ~10% of the laser power. The samples were examined using an Olympus LMPLFLN20X magnification objective, and each spectrum was obtained as ten accumulations of 10 s acquisitions. Samples were analysed by collecting spectra in triplicate, to confirm repeatability. Samples were found to be highly uniform in terms of their spectral characteristics. No background subtraction methodology was required.

Temperature-programmed reduction (H_2-TPR) experiments were carried out in an Automated Chemisorption Flow Analyzer (ChemBET Pulsar TPR/TPD, Anton Paar QuantaTec, Inc., Boynton Beach, Florida 33426, USA) under H_2 atmosphere, to acquire information on the reducibility of the samples. In a typical TPR experiment, 80 or 100 mg of sample (80 mg for the mixed oxides Co/CeO_2 and 100 mg for the ceria supports) was placed in a U-shaped quartz cell, located inside an electrical furnace, and heated up to 1100 °C at 10 deg/min under 5% H_2 in N_2 flow. To mitigate the effects of adsorbed species accumulated during storage, all samples underwent an in-situ pre-treatment in N_2 at 200 °C for 20 min prior to the TPR measurement.

X-ray Photoelectron Spectroscopy (XPS) measurements were performed using a standard, large-area XPS instrument equipped with an XR4 twin anode X-ray source, an Alpha 110 analyser, and an Ar^+ ion

gun for sample etching. The instrument also includes a sample preparation chamber, which allows for a range of *in-situ* and *in-vacuo* experiments and sample preparation procedures to minimise surface contamination prior to analysis. Survey and high-resolution spectra were collected under ultra-high vacuum conditions and the Al Kα (1486.6 eV) line was used as the excitation source. Charge neutralization was achieved using a low-energy electron flood gun when necessary. The binding energy scale was calibrated using the C 1s peak of adventitious carbon at 284.8 eV. Depth profiling was carried out using Ar^+ ion sputtering. Spectra were processed and fitted using CasaXPS with Gaussian-Lorentzian peak shapes.

Dynamic thermogravimetric analysis (TGA) of the as-synthesised materials was performed using a Rubotherm dynTHERM instrument. Gas flow was regulated with Brooks mass-flow controllers, providing a controllable range of 0–100 mL min^{-1} (STP) with an accuracy of 1% of the set point. A gas-switching manifold enabled rapid transitions between feed gases. All gases were supplied as premixed cylinders (BOC). For each measurement, 0.1 g of sample powder was loaded into the sample holder. Samples were exposed to 0.2% CO in Ar and 1% O_2 in Ar at a total flow rate of 340 mL min^{-1}. Although the CO and O_2 mole fractions were higher than those used in the catalytic tests, the CO/O_2 ratio was maintained to ensure measurable mass-change signals during TGA. Nanocubic samples were analysed from 100 °C to 550 °C, whereas nanorod samples were examined from room temperature to 200 °C, corresponding to the temperature range in which catalytic activity was observed. A heating rate of 0.5 °C min^{-1} was applied between each temperature step (of 20 °C). Gas-buoyancy effects were found to be negligible relative to the mass changes associated with oxygen release and were therefore omitted from the data analysis.

Surface analysis (XPS)

The tetravalent Co (Co^{4+}) was confirmed for all four catalysts by the u''' peak in Fig. S1a-d.[2] The trivalent Co (Co^{3+}) was confirmed via the v^0, u^0, v' and u' peaks present in every catalyst [3,4]. For CeO_2-NR, Fig. S1a, v^0, v', u^0 and u' with peaks at 884, 898 and 900 eV, respectively, correspond to Ce^{3+}.[3,4] Specifically, v' and u' resemble the Ce $3d^9$ $4f^1$ O $2p^6$ final state [3]. Also, v, v'', v''', u, u'', u''' with peaks at 882, 888, 898, 900, 907 and 916 eV correspond to Ce^{4+}, these peaks resemble a mixture between Ce $3d^9$ $4f^2$ O $2p^4$ and Ce $3d^9$ $4f^1$ O $2p^5$.[3,5] For CeO_2-NC, Fig. S1b, v^0, v', u^0 and u' with peaks at 881, 885, 897 and 902 eV respectively correspond to Ce^{3+}.[3,4] The v' and u' resemble the Ce $3d^9$ $4f^1$ O $2p^6$ final state.[3] Furthermore, v, v'', v''', u, u'', u''' with peaks at 882, 889, 898, 900, 907 and 916 eV correspond to Ce^{4+}, these peaks resemble a mixture between Ce $3d^9$ $4f^2$ O $2p^4$ and Ce $3d^9$ $4f^1$ O $2p^5$.[3,5] For Co/CeO_2-NR, Fig. S1c, v^0, v', u^0 and u' with peaks at 880, 884, 897 and 900 eV respectively correspond to Ce^{3+}.[3,4] The v' and u' resemble the Ce $3d^9$ $4f^1$ O $2p^6$ final state.[3] Also, v, v'', v''', u, u'', u''', u'''' with peaks at 882, 888, 898, 902, 907 and 916 eV correspond to Ce^{4+}, these peaks resemble a mixture between Ce $3d^9$ $4f^2$ O $2p^4$ and Ce $3d^9$ $4f^1$ O $2p^5$.[3,5] For Co/CeO_2-NC, Fig. S1d, v', u^0 and u' with peaks at 884, 897 and 900 eV, respectively, correspond to Ce^{3+}. [3,4] Specifically, v' and u' resemble the Ce $3d^9$ $4f^1$ O $2p^6$ final state.[3] Additionally, v, v'', v''', u, u'', u''', u'''' with peaks at 882, 888, 898, 902, 907 and 916 eV, respectively, correspond to Ce^{4+}, these peaks resemble a mixture between Ce $3d^9$ $4f^2$ O $2p^4$ and Ce $3d^9$ $4f^1$ O $2p^5$.[3,5] Fig. S1e and f exhibit the $Co2p_{3/2}$ peaks corresponding to the Co/CeO_2-NR and Co/CeO_2-NC samples, with the ratio of the

bivalent cobalt to trivalent cobalt (Co^{2+}/Co^{3+}) being 2.15 and 1.93, respectively. In view of this fact, the rod-shaped Co/CeO_2 catalyst with the optimum CO oxidation activity exhibits abundance in Co^{2+} sites.

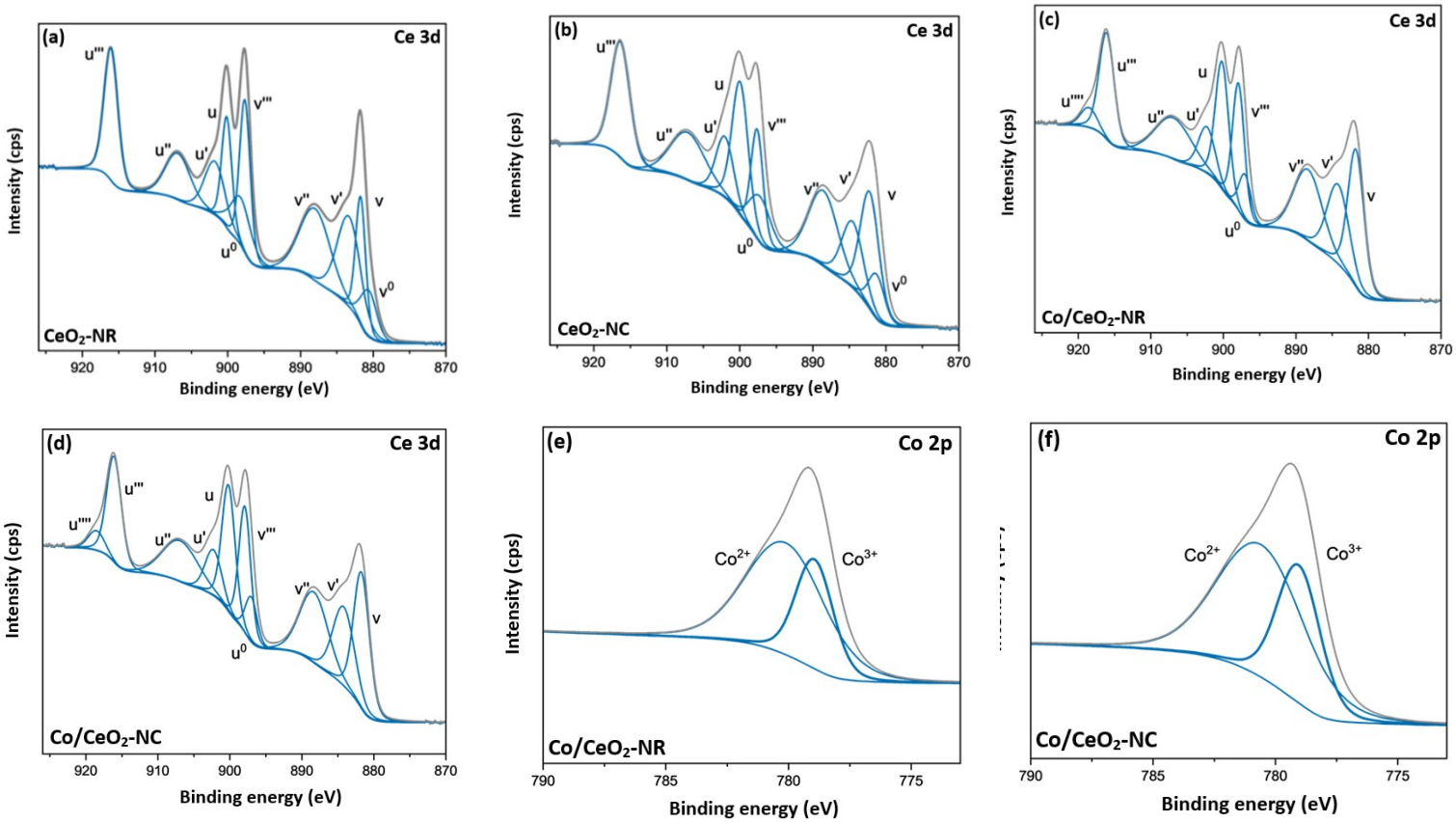

Fig. S1 Ce 3d XPS spectra of (a) CeO_2-NR, (b) CeO_2-NC, (c) Co/CeO_2-NR, (d) Co/CeO_2-NC. Co 2p XPS spectra of (e) Co/CeO_2-NR and (f) Co/CeO_2-NC.

References

1. A. Martinez Martin, S. Saini, A. Salvian, T. Miah, C. Yiu Chan, C. Avignone Rossa, S. Gadkari and K. Kousi, *Small Science*, 2025, **5**, 2400619.
2. E. Bêche, P. Charvin, D. Perarnau, S. Abanades and G. Flamant, *Surf. Inter. Anal.*, 2008, **40**, 264.
3. A. Rizzetto, M. Piumetti, R. Pirone, E. Sartoretti and S. Bensaid, *Catalysis Today*, 2024, **429**, 114478.
4. L. Li, B. Zhu, J. Zhang, C. Yan and Y. Wu, *Int. J. Hydrogen Energy*, 2018, **43**, 12909.
5. S. Watanabe, X. Ma and C. Song, *J.Phys. Chem. C*, 2009, **113**, 14249.